JACS Au
AN OPEN ACCESS JOURNAL OF THE AMERICAN CHEMICAL SOCIETY

pubs.acs.org/jacsau

Article

Hydrogen Atom Transfer Thermodynamics of Homologous Co(III)- and Mn(III)-Superoxo Complexes: The Effect of the Metal Spin State

Yao-Cheng Tian, Yang Jiang, Yen-Hao Lin, Peng Zhang, Chun-Chieh Wang, Shengfa Ye,* and Way-Zen Lee*

Cite This: *JACS Au* 2022, 2, 1899–1909

Read Online

ACCESS | Metrics & More | Article Recommendations | Supporting Information

ABSTRACT: Systematic investigations on H atom transfer (HAT) thermodynamics of metal O_2 adducts is of fundamental importance for the design of transition metal catalysts for substrate oxidation and/or oxygenation directly using O_2. Such work should help elucidate underlying electronic-structure features that govern the OO−H bond dissociation free energies (BDFEs) of metal-hydroperoxo species, which can be used to quantitatively appraise the HAT activity of the corresponding metal-superoxo complexes. Herein, the BDFEs of two homologous Co^{III}- and Mn^{III}-hydroperoxo complexes, **3-Co** and **3-Mn**, were calculated to be 79.3 and 81.5 kcal/mol, respectively, employing the Bordwell relationship based on experimentally determined pK_a values and redox potentials of the one-electron-oxidized forms, **4-Co** and **4-Mn**. To further verify these values, we tested the HAT capability of their superoxo congeners, **2-Co** and **2-Mn**, toward three different substrates possessing varying O−H BDFEs. Specifically, both metal-superoxo species are capable of activating the O−H bond of 4-oxo-TEMPOH with an O−H BDFE of 68.9 kcal/mol, only **2-Mn** is able to abstract a H atom from 2,4-di-*tert*-butylphenol with an O−H BDFE of 80.9 kcal/mol, and neither of them can react with 3,5-dimethylphenol with an O−H BDFE of 85.6 kcal/mol. Further computational investigations suggested that it is the high spin state of the Mn^{III} center in **3-Mn** that renders its OO−H BDFE higher than that of **3-Co**, which features a low-spin Co^{III} center. The present work underscores the role of the metal spin state being as crucial as the oxidation state in modulating BDFEs.

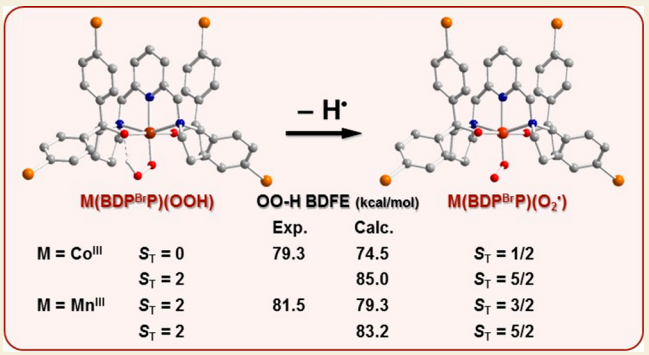

KEYWORDS: *bond dissociation free energies, hydrogen atom transfer, dioxygen activation, cobalt-superoxo complex, manganese-superoxo complex, metal spin state*

INTRODUCTION

Efficient and selective functionalization of substrates directly utilizing dioxygen, O_2, represents a desired goal of synthetic chemistry.[1] To the best of our knowledge, only a few large-scale industrial processes can realize this type of reactions, whereas such transformations have been frequently identified in the catalytic cycle of a diverse array of metalloenzymes.[2−4] In enzymatic processes, in situ generated metal-superoxo, -peroxo, and -oxo intermediates derived from O_2 activation by low-valent metal cofactors often employ hydrogen atom transfer (HAT) to oxidize their substrates. For instance, treatment of isopenicillin *N* synthase (IPNS) and myo-inositol oxygenase (MIOX) with O_2 was found to initially afford an Fe^{III}-superoxo intermediate that is capable of performing HAT reactions to produce an Fe^{III}-hydroperoxo species.[5,6] A range of metal-superoxo model compounds, such as $LCu(O_2^{\bullet})$ (L, a bis(arylcarboxamido)-pyridine ligand),[7] $(P^{Im})Fe(O_2^{\bullet})$ (P^{Im}, a porphyrinate ligand with an appended axial imidazolyl group),[8] $(P^{Ar})Fe(O_2^{\bullet})$ (P^{Ar}, a porphyrinate ligand in four varied derivatives),[9,10] $[Cu_2(XYLO)(O_2^{\bullet})]^{2+}$ (XYLO, a bis(2-{2-pyridyl}ethyl)amine chelating ligand with a bridging phenolate moiety),[11] $L'Cu_2(\mu\text{-}O_2^{\bullet})$ (L′, a tacn/pyrazolate hybrid ligand),[12] and $Co(O_2^{\bullet})(Me_3TACN)(S_2SiMe_2)$,[13] have been demonstrated to carry out HAT reactions and furnish metal-hydroperoxo complexes. Because the Gibbs free energy change of a HAT reaction can be estimated to be the difference of the X−H (X = C, N, O) bond dissociation free energy (BDFE) of the substrate relative to the OO−H BDFE of the hydroperoxo product, thermodynamically the occurrence of such a transformation requires that the latter value, as observed for all systems shown in Scheme 1, be greater than the former. Therefore, the HAT capability of a given metal-superoxo intermediate to a large extent, if not completely, depends on the OO−H BDFE of its hydroperoxo

Received: May 2, 2022
Revised: July 22, 2022
Accepted: July 22, 2022
Published: August 11, 2022

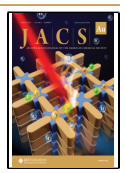

https://doi.org/10.1021/jacsau.2c00268
JACS Au 2022, 2, 1899−1909

Scheme 1. OO−H BDFEs of Biomimetic Metal-Hydroperoxo Complexes: (A) LCu(OOH),[7] (B) (P^{Im})Fe^{III}(OOH),[8] (C) (P^{Ar})Fe^{III}(OOH),[9,10] (D) [Cu_2(XYLO)(OOH)]$^{2+}$,[11] (E) L′Cu_2(μ-OOH),[12] (F) Co(OOH)(Me_3TACN)(S_2SiMe_2),[13] (G) 3-Co, and (H) 3-Mn

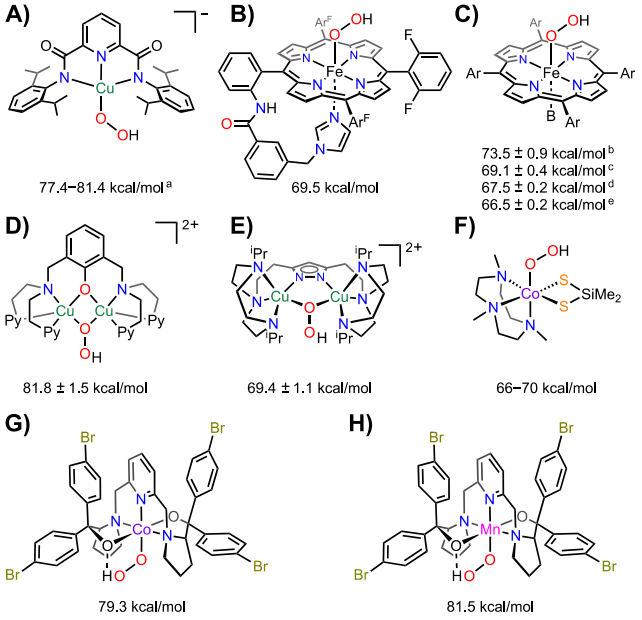

[a]Converted from BDE (83−87 kcal/mol, $C_{G,sol}$ = 66.0 kcal/mol for BDE and 60.4 kcal/mol for BDFE in THF). [b]Ar = 2,6-difluorophenyl. [c]Ar = pentafluorophenyl. [d]Ar = phenyl. [e]Ar = 2,4,6-trimethylphenyl.

product. Consequently, it is of fundamental significance to elucidate the underlying electronic-structure features that govern the OO−H BDFE, because the insights thus obtained can guide the design of transition metal catalysts that directly utilize O_2 for functionalization of substrates. Though the OO−H BDFEs of a plethora of metal-hydroperoxo species have been determined thus far (Scheme 1), systematic investigations aimed at rationalizing their varying values remain lacking.

In our long-term research work on O_2 activation mediated by the first-row transition metals, we have successfully prepared a series of Fe^{III}-, Co^{III}-, and Mn^{III}-superoxo complexes through adding O_2 to their divalent precursors at low temperatures[14−16] and explored their reactivities toward various substrates, which, in particular, demonstrated ambiphilicity of metal-superoxo species.[17,18] Specifically, Co^{III}- and Mn^{III}-superoxo complexes, Co(BDPP)($O_2^{\bullet}$) (**2′-Co**, H_2BDPP = 2,6-bis((2-(*S*)-diphenylhydroxylmethyl-1-pyrrolidinyl)methyl)pyridine), Mn(BDPP)($O_2^{\bullet}$) (**2′-Mn**), and Mn($BDP^{Br}P$)($O_2^{\bullet}$) (**2-Mn**, $H_2BDP^{Br}P$ = 2,6-bis((2-(*S*)-di(4-bromo)phenylhydroxylmethyl-1-pyrrolidinyl)methyl)pyridine), were found to react with TEMPOH to furnish the corresponding hydroperoxo complexes, Co(BDPP)(OOH) (**3′-Co**),[15] Mn^{III}(BDPP)(OOH) (**3′-Mn**),[16] and Mn^{III}($BDP^{Br}P$)(OOH) (**3-Mn**).[16] Furthermore, treatment of **2-Mn** with trifluoroacetic acid (TFA) led to formation of a Mn^{IV}-hydroperoxo complex, [Mn($BDP^{Br}P$)(OOH)]$^+$ (**4-Mn**), which could be reversibly reduced to **3-Mn**.[17] In contrast, the reaction of TFA with **2′-Co** does not result in one-electron oxidation of the metal center to yield a Co^{IV}-hydroperoxo complex, but induces protonation of the $BDPP^{2-}$ ligand and generation of [Co^{III}(HBDPP)($O_2^{\bullet}$)]$^+$ (**4′-Co**). In analogy to a HAT process, only in the presence of both electron and proton donors does transformation of **2′-Co** to **3′-Co** occur.[18]

The purpose of the present work is to investigate the HAT thermodynamics of the aforementioned Co^{III}- and Mn^{III}-superoxo complexes and clarify the electronic-structure origin for their difference. To circumvent the complexity arising from the slightly different ligand environment, we first synthesized Co($BDP^{Br}P$)($O_2^{\bullet}$) (**2-Co**) with the same ligand as **2-Mn** and then determined the OO−H BDFEs of Co($BDP^{Br}P$)(OOH) (**3-Co**) and **3-Mn**. The differential HAT capability of **2-Co** and **2-Mn** was ascertained by examining their reactions with assorted substrates having varied O−H BDFEs. Finally, density functional theory (DFT) calculations were employed to pinpoint the electronic-structure characteristics that dictate the OO−H BDFEs of **3-Co** and **3-Mn**. Our combined experimental and theoretical studies enable us, for the first time, to demonstrate that the distinct metal spin state is responsible for the varied HAT capability of the homologous Co^{III}- and Mn^{III}-superoxo complexes. Of note, the effects of the metal spin state on the HAT reaction rates of Fe^{IV}=O species have been well documented in the literature.[19−22] Furthermore, it has been reported that the different metal spin state also affects the strength of metal−NO interactions.[23] Equally important is that the metal oxidation state has been shown to play a significant role in controlling O−H BDFEs of a range of Fe-, Mn-,[24] and Cu-hydroxo[25] complexes.

RESULTS AND DISCUSSION

Synthesis of Co($BDP^{Br}P$)($O_2^{\bullet}$) (2-Co) and Determination of the OO−H BDFEs of Co($BDP^{Br}P$)(OOH) (3-Co)

To prepare the homologous Co^{III}-superoxo complex Co($BDP^{Br}P$)($O_2^{\bullet}$) (**2-Co**), a green Co^{II} starting material, Co($BDP^{Br}P$) (**1-Co**), was synthesized by reacting $H_2BDP^{Br}P$ with 1 equiv of $CoCl_2$ in the presence of NaH (2.5 equiv) in 1:1 tetrahydrofuran (THF)/CH_3CN mixed solvent (Figure S1). The molecular structure of **1-Co** determined by crystallographic analysis revealed that the Co^{II} center possesses a distorted square-pyramidal geometry with τ = 0.47 (Figure 1). The

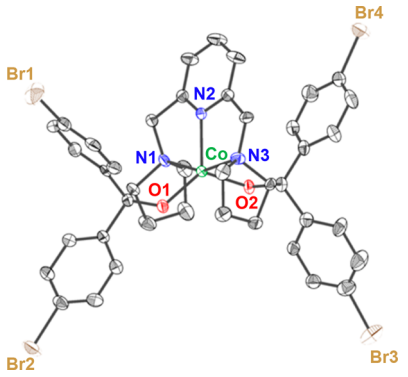

Figure 1. ORTEP of **1-Co** with ellipsoids set at 50% probability. Hydrogen atoms are omitted for clarity.

crystallographic data and the selected bond lengths and angles are listed in Tables S1 and S2. The effective magnetic moment of **1-Co** measured by the Evans method is 4.4 μ_B (Figure S2), indicative of an S_T = 3/2 ground state, similar to that found for **1′-Co**.

Upon bubbling O_2 into a THF solution of **1-Co** at −90 °C, the appearance of two characteristic absorption bands at 485 and

https://doi.org/10.1021/jacsau.2c00268
JACS Au 2022, 2, 1899−1909

570 nm in the UV−vis spectrum signaled the generation of **2-Co**, as the same features were found for the formation of **2′-Co** (Figure S1).[15] Furthermore, **2-Co** registers an almost identical EPR spectrum (Figure 2a) to **2′-Co**, reflecting that **2-Co** is

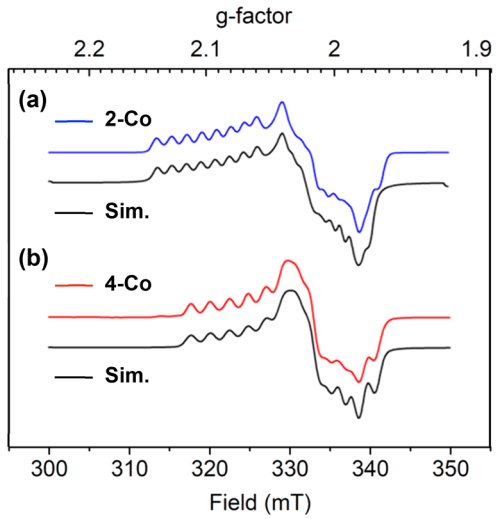

Figure 2. X-band EPR spectra of (a) **2-Co** and (b) **4-Co**. Measurement conditions: T = 100 K, f_{mw} = 9.393 and 9.410 GHz, respectively. The simulations were obtained by using the following parameters: g = 2.011, 2.097, 1.994, A_{Co} = 24, 57, 29 MHz, a = 27° for **2-Co**, and g = 2.012, 2.062, 2.003, A_{Co} = 17, 75, 20 MHz, a = 30° for **4-Co**. The definition of a is described in the Supporting Information.[26]

composed of a low-spin (S_{Co} = 0) Co^{III} center interacting with a superoxo ligand as unequivocally identified for **2′-Co**.[15] **2-Co** also performs a HAT reaction toward TEMPOH in THF at −90 °C to form a low-spin (S_{Co} = 0) Co^{III}-hydroperoxo complex, $Co(BDP^{Br}P)(OOH)$ (**3-Co**), and a TEMPO radical in 93% yield (Figures S4 and S5).

Treating **2-Co** with 1 equiv of HOTf led to protonation of the alkoxide group of the $BDP^{Br}P^{2-}$ ligand and generated $[Co^{III}(HBDP^{Br}P)(O_2^{\bullet})]^+$ (**4-Co**). In analogy to the situation found for **2′-Co** and **4′-Co**, **2-Co** and **4-Co** exhibit similar EPR spectra (Figure 2b), and two characteristic features at 480 and 640 nm of **4-Co** emerge as those found for **4′-Co** (Figure 3a). As seen in Figure 3a, **2-Co** can be retrieved by adding 1 equiv of 1,8-bis(dimethylamino)naphthalene (proton sponge) to **4-Co** as indicated by the disappearance of the signature absorption band of **4-Co** at 640 nm and the reemergence of the absorption band of **2-Co** at 485 nm. A pK_a value of 10.3 in MeTHF at −120 °C was obtained by proton sponge titration. Actually, only around 70% of **2-Co** was regenerated, as estimated by the UV−vis spectral changes of **4-Co** to **2-Co** (Figure S6). The electrochemical property of **3-Co** was also examined by performing cyclic voltammetry (CV) measurements in a n-PrCN solution vs an Ag wire reference electrode with 0.1 M NBu_4BF_4 as electrolyte. Owing to the limited solubility of the electrolyte, CV measurements of **3-Co** had to be carried out at −80 °C instead of −120 °C. A quasi-reversible 1 e^- redox event at 0.210 V ($E_{1/2}$ vs Fc/Fc^+) was found, attributed to the **3-Co**/**4-Co** couple as displayed in Figure 4a, primarily due to the partial decay of **4-Co**. With the obtained redox potential $E_{1/2}$ and pK_a, we were able to establish a thermodynamic scheme, shown in Scheme 2a, and determine the OO−H BDFE of **3-Co** to be 79.3 kcal/mol from the Bordwell relationship (eq 1,[27] $C_{G,sol}$ = 60.4 kcal/mol for BDFE in THF[28]).

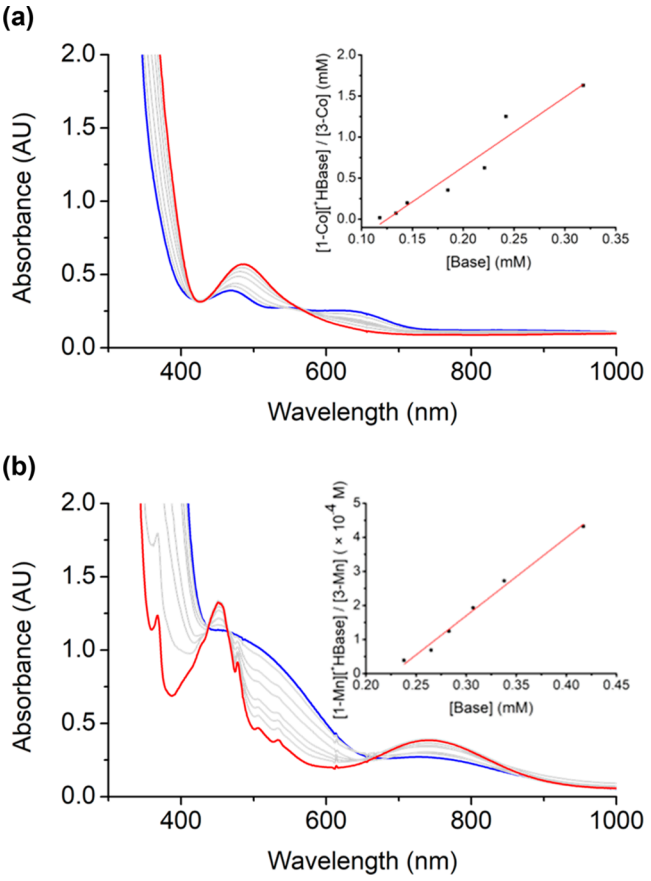

Figure 3. UV−vis spectral changes of the reactions of (a) **4-Co** and (b) **4-Mn** (1.0 mM, blue trace) with 1 equiv of base (proton sponge for **4-Co** and NEt_3 for **4-Mn**) in MeTHF at −120 °C. Inset: (a) Titration of **4-Co** provides a slope offering a K_{eq} of 5.81, which gives a pK_a value of 10.3 for **4-Co**, and (b) titration of **4-Mn** provides a slope offering a K_{eq} of 2.23, which gives a pK_a value of 12.1 for **4-Mn**.

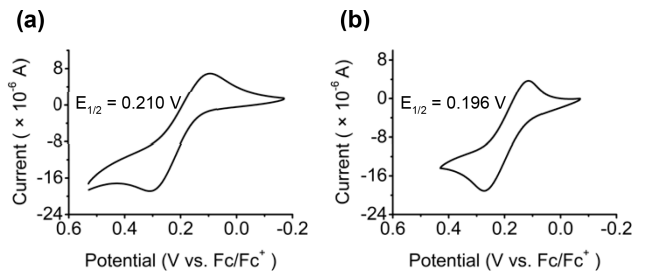

Figure 4. CV of (a) **3-Co** (1.0 mM) in n-PrCN with i_{pc}/i_{pa} = 0.63, ΔE = 215 mV (scan rate = 150 mV/s), and (b) **3-Mn** (1.0 mM) in DCM with i_{pc}/i_{pa} = 0.90, ΔE = 140 mV (scan rate = 75 mV/s) at −80 °C.

$$\mathrm{BDFE} = 1.37\mathrm{p}K_a + 23.06E^o + C_{G,sol} \quad (1)$$

Determination of the OO−H BDFE of 3-Mn

Our earlier combined spectroscopic and computational studies unequivocally established that **2-Mn** possesses a high-spin (S_{Mn} = 2) Mn^{III} center antiferromagnetically coupled with the superoxo ligand to give an overall S_T = 3/2 spin ground state.[16] Reactions of **2-Mn** with TEMPOH and trifluoroacetic acid gave hydroperoxo complexes **3-Mn** and **4-Mn** composed of a high-spin (HS, S_{Mn} = 2) Mn^{III} and a HS (S_{Mn} = 3/2) Mn^{IV} center,[17] respectively. Protonation of **2-Mn** to yield **4-Mn** was found to be reversible,[17] and the pK_a value of **4-Mn** in MeTHF at

https://doi.org/10.1021/jacsau.2c00268
JACS Au 2022, 2, 1899−1909

Scheme 2. Thermodynamic Scheme of the Discussed Co/O_2 and Mn/O_2 Species (in THF/MeTHF)

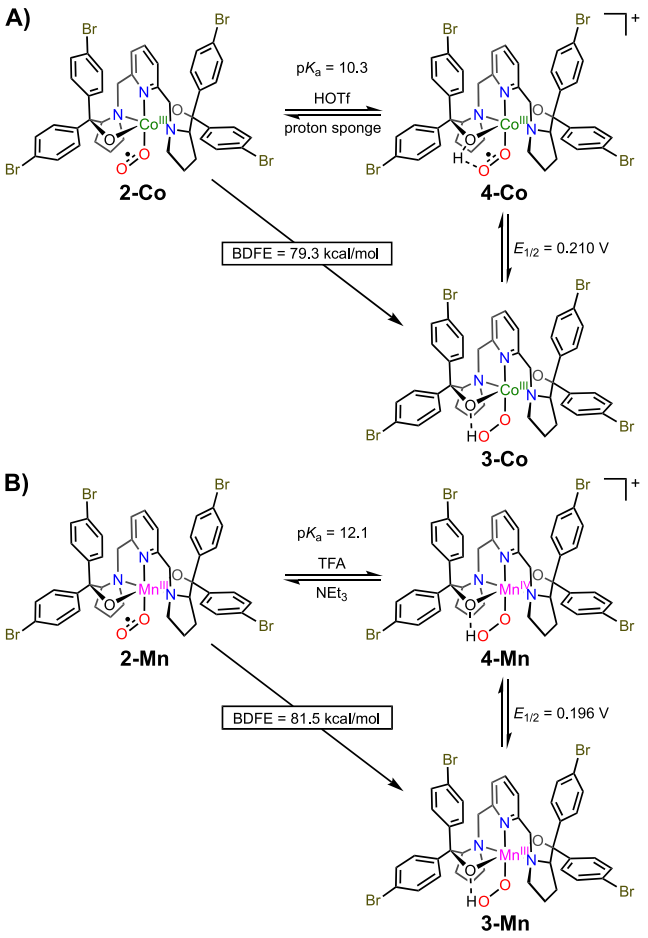

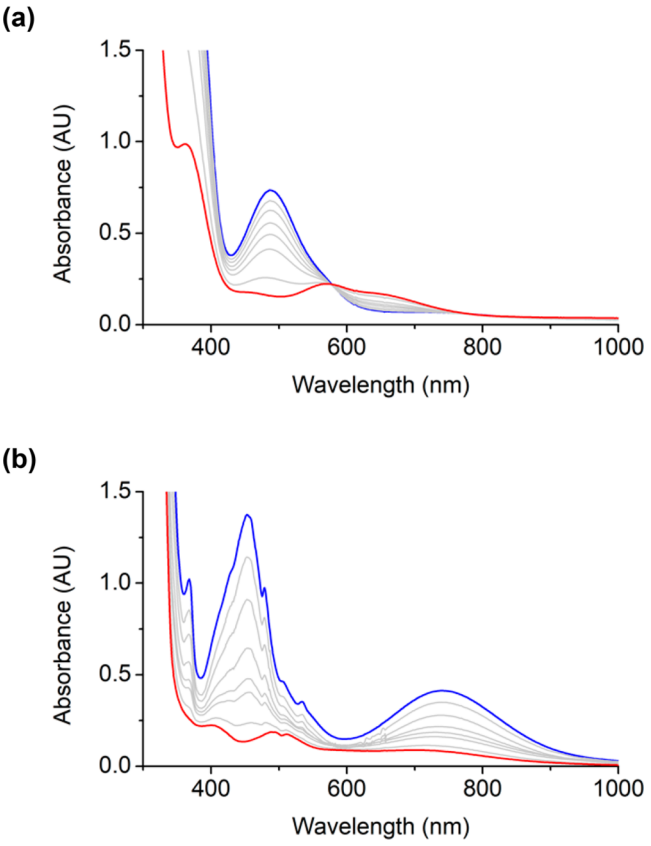

Figure 5. UV−vis spectral changes of the reaction of (A) **2-Co** and (B) **2-Mn** (1.0 mM, blue trace) with 5 equiv of 4-oxo-TEMPOH in THF at −80 °C.

−120 °C was determined to be 12.1 by NEt_3 titration, as seen in Figure 3b. Different from the **Co** system, regeneration of **2-Mn** reached a yield of 91%,[17] indicating that **4-Mn** is more stable compared to **4-Co**; therefore, CV measurements of **3-Mn** in a CH_2Cl_2 solution at −80 °C (Figure 4b) revealed a nearly reversible $1e^-$ redox wave at 0.196 V ($E_{1/2}$ vs Fc^+/Fc for **3-Mn**/**4-Mn**). On the basis of the measured $E_{1/2}$ and pK_a, the OO−H BDFE of **3-Mn** was estimated to be 81.5 kcal/mol (Scheme 2b).

Reactions of 2-Co and 2-Mn toward Substrates with Different O−H BDFEs

Owing to the thermal instability of **4-Co** and **4-Mn**, MeTHF was employed as the reaction solvent to obtain the pK_a values of **4-Co** and **4-Mn** at −120 °C; however, different solvents (n-PrCN and dichloromethane (DCM)) have to be applied for their CV measurements. In addition to these experimental limitations, $C_{G,sol}$ in THF was used to compute BDFEs; thus, we surmised that all of these factors may cause some errors in the OO−H BDFEs of **3-Co** and **3-Mn**. Therefore, three substrates with varying O−H BDFEs were employed to validate the determined OO−H BDFEs of **3-Co** and **3-Mn**. Specifically, 1-hydroxy-2,2,6,6-tetramethyl-4-oxo-piperidine (4-oxo-TEMPOH), which has an O−H BDFE (68.9 kcal/mol in THF)[28] lower than the OO−H BDFEs of **3-Co** and **3-Mn**, was selected as the first substrate for the comparison. As expected, both **2-Co** and **2-Mn** reacted with 4-oxo-TEMPOH (5 equiv) in a THF solution at −80 °C to cleanly form **3-Co** and **3-Mn** (Figure 5a and b). The organic product of 4-oxo-2,2,6,6-tetramethylpiperidine-1-oxyl radical (4-oxo-TEMPO) was detected by EPR spectroscopy in a yield of 99% for **2-Co** and 90% for **2-Mn** (Figure S9a and b). When 3,5-dimethylphenol (3,5-DMP, 10 equiv) was employed, not surprisingly, no reaction with **2-Co** or **2-Mn** occurred, because the O−H BDFE (85.6 kcal/mol in THF)[29−32] of 3,5-DMP exceeds the OO−H BDFE of **3-Co** and **3-Mn** (Figure S10a and b). When THF solutions of **2-Co** and **2-Mn** were treated by 2,4-di-*tert*-butylphenol (2,4-DTBP) at −80 °C, whose O−H BDFE (80.9 kcal/mol in THF)[29−32] is intermediate between the OO−H BDFEs of **3-Co** and **3-Mn**, no reaction was found in the mixture of **2-Co** and 2,4-DTBP (Figure 6a), whereas the HAT reaction with **2-Mn** proceeded to furnish **3-Mn** and 2,4-di-*tert*-butylphenoxyl radical as monitored by the UV−vis measurements of the reaction mixture (Figure 6b). After workup by mixing the resulting solution with HCl, the organic product of dimeric 3,3′,5,5′-tetra-*tert*-butyl-2,2′-biphenol in the resulting mixture was estimated to be in 84% yield relative to **2-Mn** by GC-MS detection (Figure S11). These experimental results clearly demonstrated that **2-Mn** is a more potent H atom abstractor than **2-Co**, in line with the varying OO−H BDFEs of **3-Co** and **3-Mn** (Scheme 3).

Calculations for BDFEs in THF

The $BDFE_{MH}$ of M−H was defined as follows:

$$BDFE_{MH} = \Delta G_{H\bullet} + \Delta G_{M\bullet} - \Delta G_{MH} \quad (2)$$

Following our earlier protocol to compute hydricity,[33,34] a property closely related to BDFE, we first chose a range of species (Table S4) with known X−H BDFEs in THF and then

https://doi.org/10.1021/jacsau.2c00268
JACS Au 2022, 2, 1899−1909

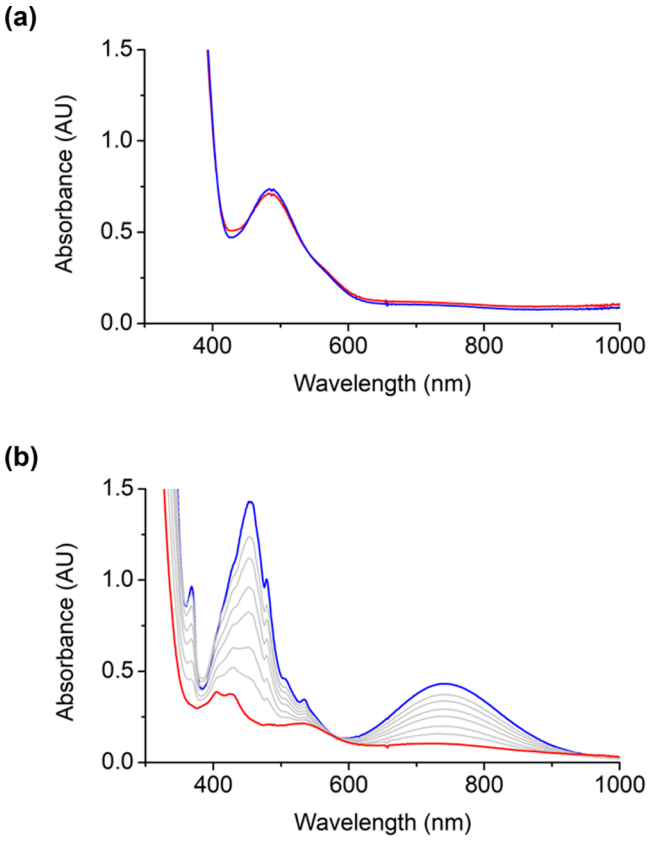

Figure 6. UV−vis spectral changes of the reactions of (a) **2-Co** and (b) **2-Mn** (1.0 mM, blue trace) with 2,4-DTBP (100 equiv) in THF at −80 °C.

Scheme 3. Reactivity of 2-Co and 2-Mn toward Three Different Substrates Possessing Varying O−H BDFEs

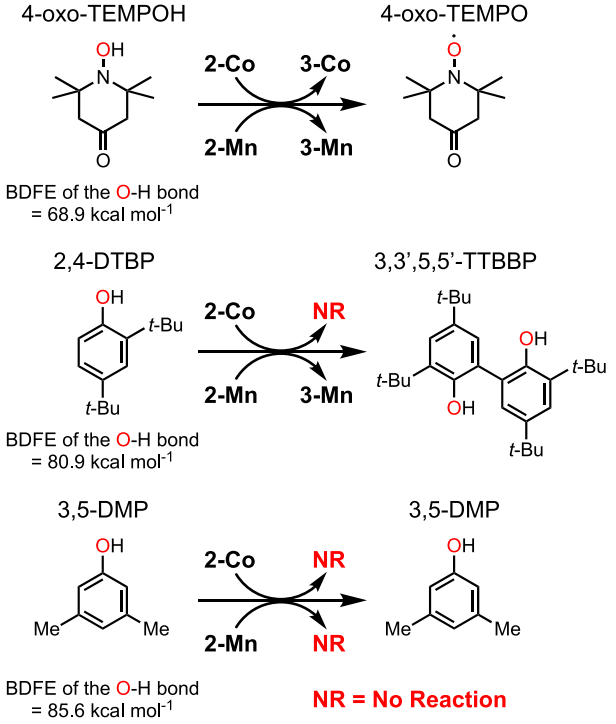

calculated their $\Delta G_{M\bullet}$ and ΔG_{MH} in THF by using the DFT approach (for details, see the Supporting Information). Finally, a linear equation between $\Delta G_{M\bullet} - \Delta G_{MH}$ and the experimental BDFE value was set up. Because $\Delta G_{H\bullet}$ in THF is a constant, it can be neglected in the linear regression analyses. The equation has a high degree of predicting power as suggested by $R^2 = 0.923$, the mean absolute error, MAE = 2.62 kcal/mol, and the root-mean-square deviation, RMSD = 3.14 kcal/mol. As a consequence, the predicted OO−H BDFEs of **3-Co** and **3-Mn** are 74.5 and 79.3 kcal/mol, respectively, which are in good agreement with the experimental values within the uncertainty range of the calculations.

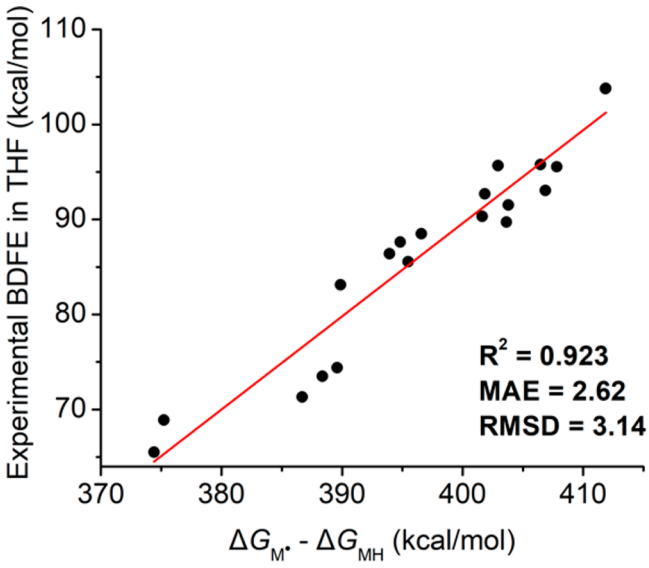

Figure 7. Correlation plot between the calculated $\Delta G_{M\bullet} - \Delta G_{MH}$ and the experimental BDFEs of a range of H atom donors in THF (for details, please refer to the Supporting Information).

DFT Calculations of HAT Thermodynamics

To gain in-depth insight into the effect of the different metal centers on the OO−H BDFEs, we chose the homolytic cleavage of the O−H bond of a hydroperoxyl radical (HOO$^\bullet$) to form a triplet dioxygen (O_2) and a hydrogen atom (H$^\bullet$), i.e., HOO$^\bullet$ → O_2 + H$^\bullet$, as the reference reaction and evaluated how the interaction of the divalent metal precursor, $M^{II}(BDP^{Br}P)$ (M = Co (**1-Co**) and Mn (**1-Mn**)), with HOO$^\bullet$ and O_2 influences the OO−H BDFE. Specifically, for a given metal, a thermodynamic cycle was set up based on the Gibbs free energy charges in THF computed for the coordination of **1-M** with HOO$^\bullet$ and O_2 to form **3-M** and **2-M**, respectively, and the difference between them ($\Delta\Delta G$) corresponds to the change in the OO−H BDFE from its original value of HOO$^\bullet$ to those found of **3-Co** and **3-Mn**.

To our knowledge, the experimental OO−H BDFE of HOO$^\bullet$ in THF has not been reported yet, but those in H_2O and DMSO are 60.6 and 58.0 kcal/mol,[35,36] respectively. As shown in Figure 8, those values are comparable to our computed ones in THF. Moreover, the OO−H BDFEs of **3-Co** and **3-Mn** (shown in maroon in Figure 8) estimated by using the thermodynamic cycle agree reasonably well with the experimental values, which suggests the reliability of this approach to dissect OO−H BDFEs.

The coordination of HOO$^\bullet$ and O_2 to both divalent metal precursors to generate the hydroperoxo and superoxo complexes

https://doi.org/10.1021/jacsau.2c00268
JACS Au 2022, 2, 1899−1909

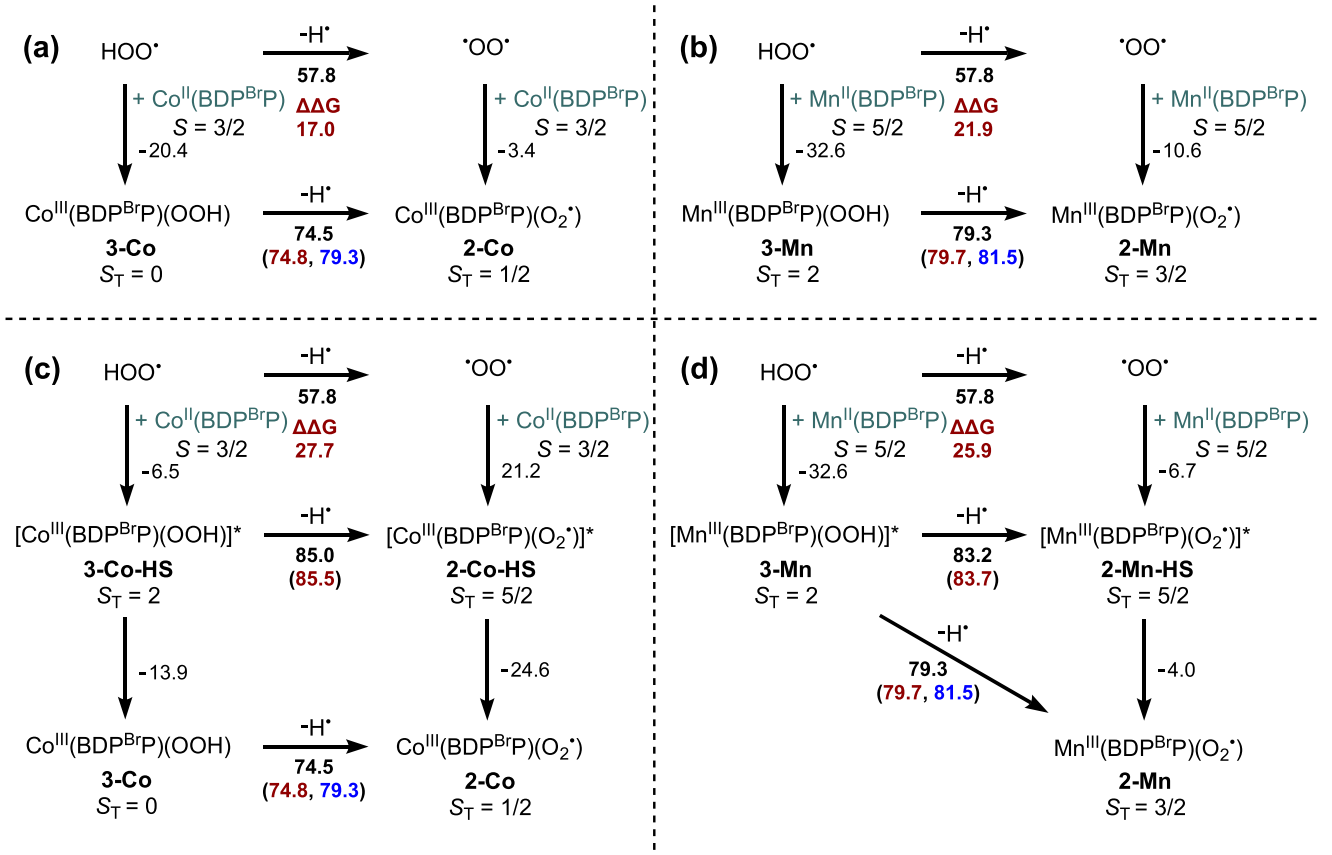

Figure 8. Thermodynamic cycles relating the BDFE of HOO• to those of (a) **3-Co**, (b) **3-Mn**, (c) **3-Co-HS**, and (d) **3-Mn-HS**. Experimental OO−H BDFEs are shown in blue, computed values based on the thermodynamic cycles are shown in maroon, and those obtained by the linear regression (Figure 7) are shown in black.

was computed to be all downhill. As elaborated for the bonding of a copper fragment to HO•,[25] such exergonicity primarily results from the overwhelming stabilizing effect of the charge transfer from the metal center to HOO• and O_2 that dominates over the e−e repulsion. Remarkably, the exergonicity of the association of O_2 was found to substantially fall behind that of the addition of HOO•. Relative to HOO• only having one π bond, O_2 possesses a pair of two-center, three-electron π bonds with two electrons occupying the π bonding orbital and one electron populating the π^* antibonding orbital. Consequently, O_2 is expected to feature a significantly higher degree of resonance stabilization than HOO•. In line with this notion is that Borden, Hoffmann, and co-workers estimated the resonance energy of O_2 to be 37 kcal/mol above that of two HOO•.[37] As such, the charge transfer from the metal center to O_2 alleviates the resonance stabilization much more pronouncedly than that to HOO•, which likely accounts for the observation that the interaction of HOO• with the divalent metal precursors is more favored than that of O_2. Consequently, the OO−H BDFEs of **3-Co** and **3-Mn** appreciably exceed that found for HOO•. Specifically, interaction of HOO• and O_2 with **1-Co** to generate **3-Co** and **2-Co** is exergonic by −20.4 and −3.4 kcal/mol, respectively; thus $\Delta\Delta G$ = 17.0 kcal/mol. The corresponding values for **3-Mn** and **2-Mn** are −32.6 and −10.6 kcal/mol; thus, $\Delta\Delta G$ = 21.9 kcal/mol. The more positive $\Delta\Delta G$ computed for the Mn system ultimately leads to a greater OO−H BDFE of **3-Mn**.

To probe the effect of the hydrogen bond between the hydroperoxo ligand and the alkoxide group of the $BDP^{Br}P^{2-}$ ligand in **3-Co** and **3-Mn**, we calculated the corresponding hypothetical hydroperoxo models in which the H atom of the OOH ligand points upward and hence has vanishing interaction with the supporting ligand. The thus-obtained OO−H BDFE of the Mn complex (72.0 kcal/mol) still surpasses that of the Co complex (67.7 kcal/mol).

Comparing the electronic structures of **3-Co** and **3-Mn**, we surmised that the metal spin state is likely a determinant of their differential OO−H BDFEs. To verify this hypothesis, we initially aimed to compute a hypothetical quartet model consisting of an S_{Co} = 2 Co^{III} center antiferromagnetically coupled to a superoxo radical, which features a similar electronic structure to **2-Mn**. Despite repeated attempts, the calculations did not converge to the desired electronic structure, but to an S_{Co} = 1 Co^{III} center that is ferromagnetically coupled to a superoxo radical. Gratifyingly, when the interaction of the two fragments was transitioned from antiferromagnetic coupling to ferromagnetic coupling, we succeeded in locating a sextet model (**2-Co-HS**). On top of that, we estimated the OO−H BDFE of its corresponding S_T = 2 hydroperoxo species (**3-Co-HS**). To make a reasonable comparison, we also calculated the OO−H BDFE of **3-Mn** with respect to **2-Mn-HS** (**3-Mn**/**2-Mn-HS**) in which a HS Mn^{III} center (S_{Mn} = 2) is ferromagnetically coupled to a superoxo radical ligand. All theoretical results are summarized in Figure 8.

The calculations predicted that the OO−H BDFE of **3-Mn**/**2-Mn-HS** slightly surpasses that of **3-Mn**/**2-Mn** by only 4.0 kcal/mol, whereas the difference between the OO−H BDFE of **3-Co-HS**/**2-Co-HS** and that of **3-Co**/**2-Co** is as large as 10.5 kcal/

https://doi.org/10.1021/jacsau.2c00268
JACS Au 2022, 2, 1899−1909

mol. Of note, the former energy gap is close to the uncertainty range of our computations, but the latter is far beyond that. More importantly, when both metal centers are in the HS state, the computed OO−H BDFEs of **3-Co-HS**/**2-Co-HS** and **3-Mn**/**2-Mn-HS** are comparable. However, upon going from **2-Co-HS** and **3-Co-HS** to **2-Co** and **3-Co**, respectively, the changes of the Co spin state impart a markedly higher degree of the stabilization to the superoxo complex (−24.6 kcal/mol) than that to the hydroperoxo complex (−13.9 kcal/mol), which lowers the OO−H BDFE of **3-Co** below that of **3-Mn** in the end.

Electronic−Structure Analyses

During the formation of **2-Co-HS**, in order to retain the Co HS state, the Co^{II} center in **1-Co** needs to transfer a β electron to the O_2 π^* orbital; therefore, the electron-donating orbital has to be one of the doubly populated t_{2g}-derived orbitals of the Co^{II} center (Figure 9). As depicted in Figure 10, in **2-Co-HS** the O_2

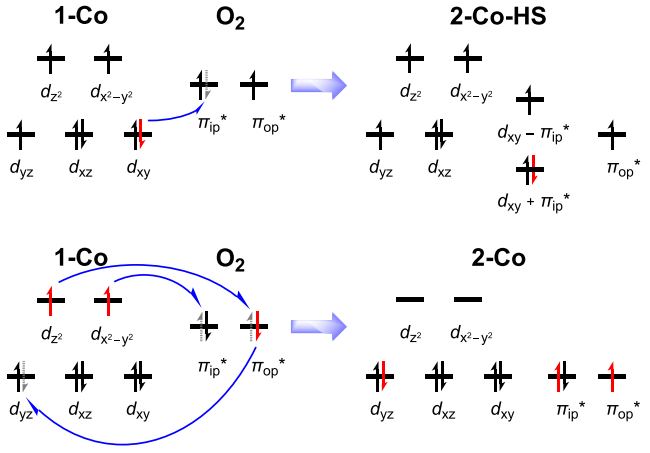

Figure 9. Schematic electronic-structure evolution for the formation of **2-Co-HS** and **2-Co** by adding O_2 to **1-Co**.

π_{ip}^* orbital in the Co−O−O plane interacts primarily with Co d_{xy} to form a pseudo σ bond, because both fragment orbitals do not have optimal symmetry for efficient overlap. More importantly, the thus-generated bonding and antibonding molecular orbitals (MOs) labeled as $d_{xy} + \pi_{op}^*$ and $d_{xy} - \pi_{op}^*$, respectively, have almost equal parentage of O_2 and Co. As such, O_2 coordination is accompanied by a partial electron transfer from the Co^{II} center of **1-Co** to the incoming O_2 ligand. Furthermore, together with the singly populated O_2 π_{op}^* MO perpendicular to the Co−O−O plane, the electronic structure of **2-Co-HS** is hence best interpreted as a resonance hybrid ranging between HS Co^{II}−O_2 and HS Co^{III}−$O_2^{\bullet}$.

Different from that of **2-Co-HS**, the electronic-structure evolution for the generation of **2-Co** can be formally interpreted as follows. Upon O_2 approaching the Co^{II} center in **1-Co**, the latter species shifts two α electrons in the e_g set into the two O_2 π^* orbitals, which is concurrent with transfer of a β electron from the O_2 π_{op}^* to a Co t_{2g}-derived orbital. As a consequence, the Co center of the resulting **2-Co** complex possesses a low-spin state with two completely empty Co $d_{x^2-y^2}$ and d_{z^2} orbitals. In **2-Co** the O_2 π_{ip}^* orbital exclusively interacts with the Co d_{x2-y2} orbital, because both fragment orbitals have appropriate symmetry and their overlap is more efficient than the Co−O_2 quasi σ bond found for **2-Co-HS** involving Co d_{xy} and O_2 π_{ip}^*. For **2-Co**, in addition to two electrons occupying the O_2 π_{ip}^* orbital, one electron resides in the O_2 π_{op}^* MO. This orbital occupation pattern therefore defines an authenticated superoxo ligand in **2-Co** and suggests that the aforementioned electron transfer has already occurred. Consistent with this notion, the computed Chelpg charge[38] for the O_2 ligand of **2-Co-HS** is appreciably lower than that of **2-Co**, and the same trend was also found for Mulliken and Löwdin charges (for details, please refer to Figures S12−14 in the Supporting Information). The ease of the Co-to-O_2 electron transfer in the formation of **2-Co** and **2-Co-HS** can be ultimately traced back to the differential energy of the employed Co donating orbitals (EDOs). For **2-Co**, one of the high-energy e_g-derived orbitals functions as the EDO, whereas for **2-Co-HS** a low-energy t_{2g}-derived orbital acts as the EDO. Although the Co−O_2 π interactions involving the Co d_{xz} and O_2 π_{op}^* fragment orbitals are almost the same for both superoxo species, the flip of the Co spin state replaces an approximately half pseudo σ bond in **2-Co-HS** formed by Co d_{xy} and O_2 π_{ip}^* with a σ bond in **2-Co** formed by Co $d_{x^2-y^2}$ and O_2 π_{ip}^*. This electronic-structure change thus induces considerable shortening of the Co−O_2 bond distance found for **2-Co** relative to **2-Co-HS**.

Upon going from **2-Co** to **3-Co**, due to the interaction with the proton, the originally doubly populated O_2 π_{op} and π_{op}^* orbitals split into a lone pair that interacts with the metal center and an OO−H σ bonding orbital. Comparison of the estimated charges of the HOO moiety of **3-Co-HS** and **3-Co** showed that lowering the Co spin state also induces more favorable electron transfer from the metal center to $HOO^{\bullet}$. This is primarily due to the covalent Co−OOH π interaction in **3-Co-HS**; therefore, three electrons are delocalized into the Co d_{xz} and HOO π_{op}^* fragment orbitals, which thus defines a half Co−OOH π bond. Because **3-Co-HS** features a HS state, its Co $d_{x^2-y^2}$ orbital is singly occupied, which results in a half σ Co−OOH bond formed by Co $d_{x^2-y^2}$ and HOO π_{ip}^*. The Co−OOH bonding strength of **3-Co-HS** is hence more or less the same as that of **3-Co**, having mere one Co−OOH σ interaction, consistent with their nearly identical Co−OOH bond lengths. As such, one can conclude that the change of the Co spin state results in more pronounced electronic-structure changes in the superoxo complexes than those in the hydroperoxo complexes; consequently, the exergonicity computed for **2-Co-HS** → **2-Co** exceeds that for **3-Co-HS** → **3-Co**, which reduces the OO−H BDFE from 85.0 kcal/mol for **3-Co-HS** to 74.5 kcal/mol for **3-Co**. Taken together, the distinct metal spin state of homologous **3-Co** and **3-Mn** complexes is the main reason for their varying OO−H BDFEs.

CONCLUSION

We report here the HAT thermodynamics of the homologous Co^{III}- and Mn^{III}-superoxo species **2-Co** and **2-Mn** in THF. Both complexes can be reversibly protonated to yield **4-Co** and **4-Mn**, which undergo reversible one-electron reduction to generate the corresponding Co^{III}- and Mn^{III}-hydroperoxo complexes **3-Co** and **3-Mn**. The redox potentials of **3-Co** and **3-Mn** and the pK_a values of **4-Co** and **4-Mn** have been directly determined by CV measurements and titration experiments. On the basis of them, the OO−H BDFEs of **3-Co** and **3-Mn** were estimated to be 79.3 and 81.5 kcal/mol, respectively, by using the thermodynamic scheme and Bordwell relationship. It has been experimentally shown that **2-Mn** is capable of abstracting H atoms from 4-oxo-TEMPOH with an O−H BDFE of 68.9 kcal/mol and 2,4-DTBP with an O−H BDFE of 80.9 kcal/mol, but failed to activate the O−H bond of 3,5-DMP with an O−H BDFE of 85.6 kcal/mol, while **2-Co** can react only with 4-oxo-TEMPOH. These

https://doi.org/10.1021/jacsau.2c00268
JACS Au 2022, 2, 1899−1909

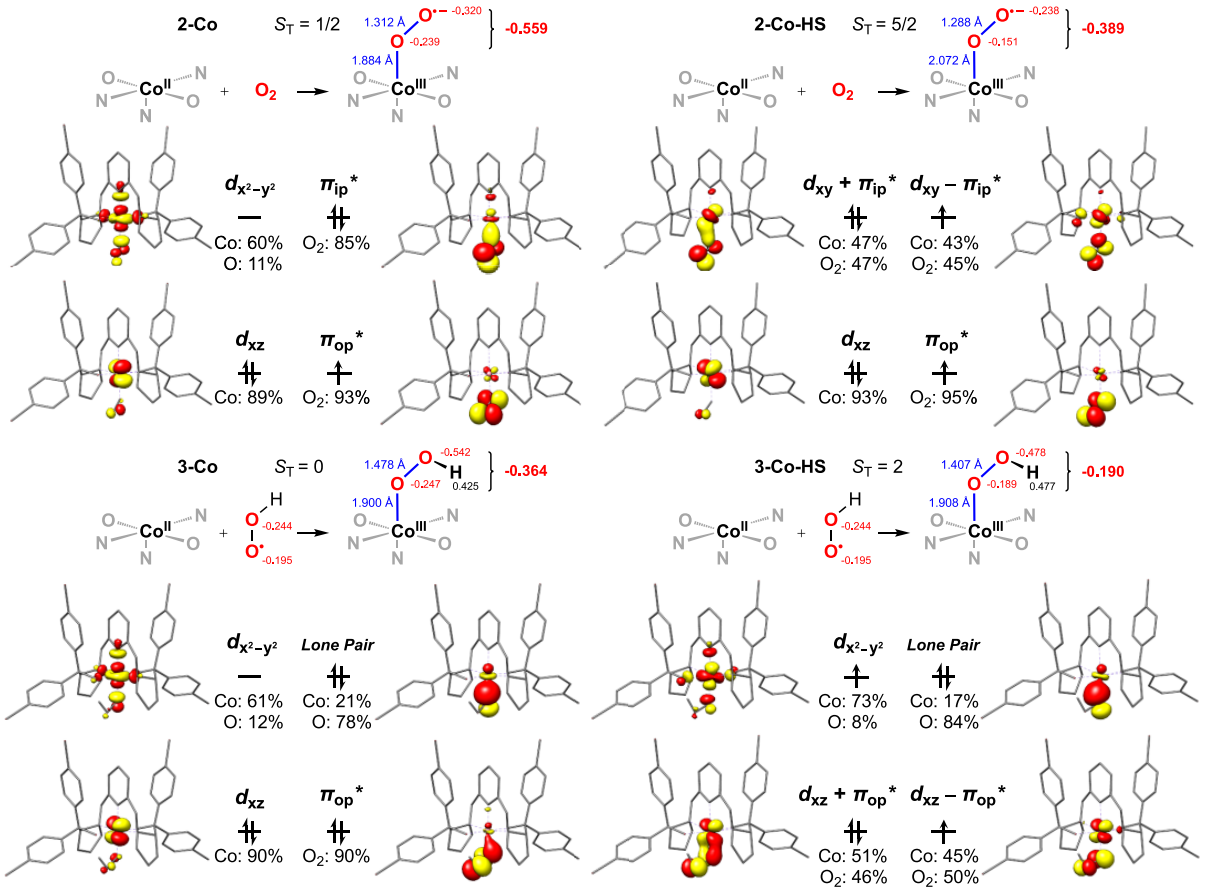

Figure 10. Comparison of the geometric- and electronic-structure changes upon addition of HOO$^{\bullet}$ and O_2 to **1-Co** to generate **3-Co**, **3-Co-HS**, **2-Co**, and **2-Co-HS** and molecular orbitals describing Co−OOH and Co−O_2 interactions thereof. Red numbers are Chelpg charges computed for the O_2 and OOH ligands.

experimental findings thus affirmed the calculated OO−H BDFEs of **3-Co** and **3-Mn**. To probe the effect of the metal spin state on OO−H BDFEs, we computationally investigated the corresponding hypothetical high-spin Co^{III}-superoxo and -hydroperoxo complexes **2-Co-HS** and **3-Co-HS**. Detailed theoretical analyses showed that **2-Co-HS** features weaker $Co^{III}-O_2^{-\bullet}$ interactions relative to **2-Co**, because in formation of **2-Co-HS** a low-energy t_{2g}-derived orbital serves as the EDO that reluctantly donates the electron into O_2, whereas a high-energy e_g-derived orbital functions as the EDO in the generation of **2-Co**. Hence, **3-Co-HS** possesses a much stronger OO−H bond than **3-Co** and even surpasses that of **3-Mn**. A different metal spin state is therefore responsible for the varying OO−H BDFEs of **3-Co** and **3-Mn**. The present work for the first time pinpoints, in addition to the metal oxidation state, the metal spin state, which is another crucial factor governing BDFEs. Therefore, our findings would add a new dimension to the design of transition metal systems that catalyze functionalization of substrates directly using O_2 as the oxidant.

EXPERIMENTAL SECTION

Materials and Methods

All manipulations were operated under a nitrogen or argon atmosphere using standard Schlenk techniques or in a glovebox. Acetonitrile and dichloromethane were distilled under nitrogen over CaH_2 prior to use; THF, MeTHF, pentane, and diethyl ether were purified by Na/benzophenone and distilled prior to use. n-PrCN was purified using Na_2CO_3 and $KMnO_4$ and then distilled prior to use. Mn(BDP^{Br}P) (**1-Mn**), Mn(BDP^{Br}P)($O_2^{\bullet}$) (**2-Mn**), Mn(BDP^{Br}P)(OOH) (**3-Mn**), [Mn(BDP^{Br}P)(OOH)]$^+$ (**4-Mn**), 1-hydroxy-2,2,6,6-tetramethylpiperidine, and 1-hydroxy-2,2,6,6-tetramethyl-4-oxo-piperidine were prepared by utilizing the method reported previously.[16,17,39−41] Other chemical reagents were obtained from commercial sources and used as received unless stated otherwise. UV−vis spectra were recorded with an Agilent 8454 spectrophotometer equipped with a cryostat from Unisoku Scientific Instruments, Osaka, Japan. Product analyses were performed with an Agilent GC6890 gas chromatograph (GC-MS). Elemental analyses for C, H, and N were performed on an Elementar Vario EL cube analyzer at the Instrumentation Center at National Taiwan University.

Synthesis of Co(BDP^{Br}P) (1-Co)

1-Co was synthesized by reacting $CoCl_2$ (26.0 mg, 0.2 mmol) with H_2BDP^{Br}P (184.6 mg, 0.2 mmol) and NaH (12.0 mg, 0.5 mmol) in 1:1 THF/CH_3CN mixed solvent (20 mL) in a 50 mL Schlenk flask. The solution was stirred for 12 h at ambient temperature, and the solvent was removed under vacuum. The green residue was dissolved in CH_2Cl_2 (15 mL) and filtered. The filtrate was concentrated under vacuum and recrystallized by slow diffusion of Et_2O into the concentrated THF filtrate at ambient temperature. Green crystals of **1-Co** were obtained over 1 day in 62% yield. The molecular structure of **1-Co** features a distorted square pyramidal geometry (τ_5 = 0.47). UV−vis (THF): 375 nm (306 M^{-1} cm^{-1}). Anal. Calcd for $C_{41}H_{41}Br_4CoN_3O_2 \cdot C_4H_8O$ (FW = 1054.41): C, 51.26; H, 4.30; N, 3.99. Found: C, 51.649; H, 4.432; N, 4.048.

Formation of Co(BDP^{Br}P)($O_2^{\bullet}$) (2-Co)

Complex **2-Co** was generated by bubbling O_2 into a THF solution of **1-Co** at −90 °C from an oxygen balloon for 2 min. Formation of **2-Co** was

https://doi.org/10.1021/jacsau.2c00268
JACS Au 2022, 2, 1899−1909

monitored by UV−vis spectroscopy on characteristic absorption bands of **2-Co** at 485 and 570 nm (Figure S1).

Formation of Co(BDP^{Br}P)(OOH) (3-Co)

Reaction of **2-Co** with excess TEMPOH in THF at −90 °C gave a deep blue solution of **3-Co**, which displayed three absorption bands at 375, 580, and 640 nm (Figure S4).

X-ray Data Collection and Structure Determination

X-ray diffraction data of **1-Co** was collected on a Bruker D8 Venture diffractometer employing Mo Kα radiation (λ = 0.7107 Å) at 200 K and with a θ−2θ scan mode. The space group for **1-Co** was determined on the basis of systematic absences and intensity statistics. Their structures were solved by direct methods using SIR92 or SIR97 and refined using SHELXL-97 with anisotropic displacement factors for all non-hydrogen atoms. The detailed crystallographic data of **1-Co** were provided in its CIF file.

EPR Measurements

X-Band CW EPR measurements were performed at the temperature of 100 K using a Bruker EMXmicro-6/1/S/L spectrometer equipped with a Bruker E4119001 HS-W1 resonator and Bruker E7003500 temperature controller. Microwave power was in the range of 17 to 20 mW. The magnetic field modulation amplitude was 10 G. Simulations with an S = 1/2 spin Hamiltonian including an electronic Zeeman term and a ^{59}Co hyperfine interaction were carried out with EasySpin.[42]

Computational Setup

All computations were performed with the ORCA-4.2.0 program package.[43] Geometry optimizations were performed by using the PBE[44] functional in combination with the D3BJ noncovalent corrections.[45,46] The triple-ζ def2-TZVP basis set was used for the first coordination sphere, and the def2-SVP basis set for the remaining atoms.[47−49] Solvation effects were accounted for by the CPCM model[50] with THF being the solvent. To reduce computational costs, the resolution of identity (RI) approximation in tandem with the def2/J auxiliary basis set was employed.[51] Due to difficulties of SCF convergence in some cases, damping parameters were altered using the SlowConv function in ORCA. Frequency calculations confirmed that all optimized structures had converged to local minima on the potential energy surface (i.e., no imaginary frequencies). The PBE density functional is employed for geometry optimizations and frequency analyses, because, in addition to the high computational efficiency, calculations with GGA density functionals often deliver reliable structures and frequencies.[52,53] Final single-point calculations of electronic energies were carried out by using the TPSSh,[54] B3LYP,[55,56] and BP86 functionals[57,58] with the def2-TZVPP basis set for all atoms[59] and then benchmarked by DLPNO-CCSD(T) computations.[60,61] As elaborated in the Supporting Information, TPSSh gives the most satisfactory results of O−H BDFEs, as found in an earlier study.[25]

■ ASSOCIATED CONTENT

Supporting Information

The Supporting Information is available free of charge at https://pubs.acs.org/doi/10.1021/jacsau.2c00268.

UV−vis, ^{1}H NMR, EPR and GC-MS spectra, X-ray data, and computational details and coordinates (PDF)

Detailed crystallographic data of **1-Co** (CIF)

■ AUTHOR INFORMATION

Corresponding Authors

Way-Zen Lee − *Department of Chemistry, National Taiwan Normal University, Taipei 11677, Taiwan; Department of Medicinal and Applied Chemistry, Kaohsiung Medical University, Kaohsiung 807, Taiwan;* orcid.org/0000-0003-0053-1621; Email: wzlee@ntnu.edu.tw

Shengfa Ye − *State Key Laboratory of Catalysis, Dalian Institute of Chemical Physics, Chinese Academy of Sciences, Dalian 116023, China;* orcid.org/0000-0001-9747-1412; Email: shengfa.ye@dicp.ac.cn

Authors

Yao-Cheng Tian − *Department of Chemistry, National Taiwan Normal University, Taipei 11677, Taiwan*

Yang Jiang − *State Key Laboratory of Catalysis, Dalian Institute of Chemical Physics, Chinese Academy of Sciences, Dalian 116023, China*

Yen-Hao Lin − *Department of Chemistry, National Taiwan Normal University, Taipei 11677, Taiwan*

Peng Zhang − *State Key Laboratory of Catalysis, Dalian Institute of Chemical Physics, Chinese Academy of Sciences, Dalian 116023, China; University of Chinese Academy of Sciences, Beijing 100049, China*

Chun-Chieh Wang − *Department of Chemistry, National Taiwan Normal University, Taipei 11677, Taiwan*

Complete contact information is available at: https://pubs.acs.org/10.1021/jacsau.2c00268

Author Contributions

Y.-C.T. and Y.J. contributed equally to the present work.

Notes

The authors declare no competing financial interest.

■ ACKNOWLEDGMENTS

We thank the Instrumentational Center of National Taiwan Normal University, Department of Chemistry, for EPR measurements. The authors are grateful for the financial support from the Ministry of Science and Technology of Taiwan (MOST 108-2113-M-003-009-MY3 to W.-Z.L.).

■ REFERENCES

(1) Bertini, I.; Gray, H. B.; Lippard, S. J.; Valentine, J. S. *Dioxygen Reactions. Bioinorganic Chemistry*; University Science Books: Mill Valley, CA, 1994; pp 253−313.

(2) Sheldon, R. A.; Kochi, J. K. *Metal Catalyzed Oxidations of Organic Compound*; Academic Press: New York, 1981.

(3) Hill, C. L. In *Advances in Oxygenated Processes*, Vol. *1*; Baumstark, A. L., Eds.; JAI Press: London, 1988; p 1.

(4) Hudlucky, M. *Oxidations in Organic Chemistry*; ACS Monograph Series; American Chemical Society: Washington, DC, 1990.

(5) Tamanaha, E.; Zhang, B.; Guo, Y.; Chang, W.-c.; Barr, E. W.; Xing, G.; St. Clair, J.; Ye, S.; Neese, F.; Bollinger, J. M., Jr.; Krebs, C. Spectroscopic Evidence for the Two C−H-Cleaving Intermediates of Aspergillus nidulans Isopenicillin N. *J. Am. Chem. Soc.* **2016**, *138* (28), 8862−8874.

(6) Xing, G.; Diao, Y.; Hoffart, L. M.; Barr, E. W.; Prabhu, K. S.; Arner, R. J.; Reddy, C. C.; Krebs, C.; Bollinger, J. M. Evidence for C-H cleavage by an iron-superoxide complex in the glycol cleavage reaction catalyzed by myo-inositol oxygenase. *Proc. Natl. Acad. Sci. U.S.A.* **2006**, *103* (16), 6130−6135.

(7) Bailey, W. D.; Dhar, D.; Cramblitt, A. C.; Tolman, W. B. Mechanistic Dichotomy in Proton-Coupled Electron-Transfer Reactions of Phenols with a Copper Superoxide Complex. *J. Am. Chem. Soc.* **2019**, *141*, 5470−5480.

(8) Kim, H.; Rogler, P. J.; Sharma, S. K.; Schaefer, A. W.; Solomon, E. I.; Karlin, K. D. Ferric Heme Superoxide Reductive Transformations to Ferric Heme (Hydro)Peroxide Species: Spectroscopic Characterization and Thermodynamic Implications for H-Atom Transfer (HAT). *Angew. Chem., Int. Ed.* **2021**, *60*, 5907−5912.

(9) Kim, H.; Rogler, P. J.; Sharma, S. K.; Schaefer, A. W.; Solomon, E. I.; Karlin, K. D. Heme-Fe^{III} Superoxide, Peroxide and Hydroperoxide

Thermodynamic Relationships: Fe^{III}-$O_2^{\bullet-}$ Complex H-Atom Abstraction Reactivity. *J. Am. Chem. Soc.* **2020**, *142*, 3104−3116.
(10) Mondal, P.; Ishigami, I.; Gérard, E. F.; Lim, C.; Yeh, S.-R.; de Visser, S. P.; Wijeratne, G. B. Proton-coupled electron transfer reactivities of electronically divergent heme superoxide intermediates: a kinetic, thermodynamic, and theoretical study. *Chem. Sci.* **2021**, *12*, 8872−8883.
(11) Quist, D. A.; Ehudin, M. A.; Schaefer, A. W.; Schneider, G. L.; Solomon, E. I.; Karlin, K. D. Ligand Identity-Induced Generation of Enhanced Oxidative Hydrogen Atom Transfer Reactivity for a $Cu^{II}_2(O_2^{\bullet-})$ Complex Driven by Formation of a $Cu^{II}_2(^{-}OOH)$ Compound with a Strong O−H Bond. *J. Am. Chem. Soc.* **2019**, *141*, 12682−12696.
(12) Kindermann, N.; Günes, C.-J.; Dechert, S.; Meyer, F. Hydrogen Atom Abstraction Thermodynamics of a μ-1,2-Superoxo Dicopper(II) Complex. *J. Am. Chem. Soc.* **2017**, *139*, 9831−9834.
(13) Gordon, J. B.; Vilbert, A. C.; Siegler, M. A.; Lancaster, K. M.; Moënne-Loccoz, P.; Goldberg, D. P. A Nonheme Thiolate-Ligated Cobalt Superoxo Complex: Synthesis and Spectroscopic Characterization, Computational Studies, and Hydrogen Atom Abstraction Reactivity. *J. Am. Chem. Soc.* **2019**, *141*, 3641−3653.
(14) Chiang, C. W.; Kleespies, S. T.; Stout, H. D.; Meier, K. K.; Li, P. Y.; Bominaar, E. L.; Que, L., Jr.; Münck, E.; Lee, W. Z. Characterization of a Paramagnetic Mononuclear Nonheme Iron-Superoxo Complex. *J. Am. Chem. Soc.* **2014**, *136*, 10846−10849.
(15) Wang, C. C.; Chang, H. C.; Lai, Y. C.; Fang, H.; Li, C. C.; Hsu, H. K.; Li, Z. Y.; Lin, T. S.; Kuo, T. S.; Neese, F.; Ye, S.; Chiang, Y. W.; Tsai, M. L.; Liaw, W. F.; Lee, W. Z. Structurally Characterized Nonheme Cobalt−Hydroperoxo Complex Derived from Its Superoxo Intermediate via Hydrogen Atom Transfer. *J. Am. Chem. Soc.* **2016**, *138*, 14186−14189.
(16) Lin, Y. H.; Cramer, H. H.; van Gastel, M.; Tsai, Y. H.; Chu, C. Y.; Kuo, T. S.; Lee, I. R.; Ye, S.; Bill, E.; Lee, W. Z. Mononuclear Manganese(III) Superoxo Complexes: Synthesis, Characterization, and Reactivity. *Inorg. Chem.* **2019**, *58*, 9756−9765.
(17) Lin, Y.-H.; Kutin, Y.; van Gastel, M.; Bill, E.; Schnegg, A.; Ye, S.; Lee, W.-Z. A Manganese(IV)-Hydroperoxo Intermediate Generated by Protonation of the Corresponding Manganese(III)-Superoxo Complex. *J. Am. Chem. Soc.* **2020**, *142*, 10255−10260.
(18) Chen, T.-Y.; Ho, P.-H.; Spyra, C.-J.; Meyer, F.; Bill, E.; Ye, S.; Lee, W.-Z. Ambiphilicity of a Mononuclear Cobalt(III) Superoxo Complex. *Chem. Commun.* **2020**, *56*, 14821−14824.
(19) Kupper, C.; Mondal, B.; Serrano-Plana, J.; Klawitter, I.; Neese, F.; Costas, M.; Ye, S.; Meyer, F. Nonclassical Single-State Reactivity of an Oxo-Iron(IV) Complex Confined to Triplet Pathways. *J. Am. Chem. Soc.* **2017**, *139*, 8939−8949.
(20) Decker, A.; Rohde, J.-U.; Klinker, E. J.; Wong, S. D.; Que, L.; Solomon, E. I. Spectroscopic and quantum chemical studies on low-spin Fe^{IV}=O complexes: Fe-O bonding and its contributions to reactivity. *J. Am. Chem. Soc.* **2007**, *129*, 15983−15996.
(21) Shaik, S.; Chen, H.; Janardanan, D. Exchange-enhanced reactivity in bond activation by metal-oxo enzymes and synthetic reagents. *Nat. Chem.* **2011**, *3*, 19−27.
(22) Ye, S.; Neese, F. Nonheme oxo-iron(IV) intermediates form an oxyl radical upon approaching the C-H bond activation transition state. *Proc. Natl. Acad. Sci. U.S.A.* **2011**, *108*, 1228−1233.
(23) Mariusz, R. Role of Spin States in Nitric Oxide Binding to Cobalt(II) and Manganese(II) Porphyrins. Is Tighter Binding Always Stronger? *Inorg. Chem.* **2015**, *54*, 5634−5645.
(24) Gupta, R.; Borovik, A. S. Monomeric $Mn^{III/II}$ and $Fe^{III/II}$ Complexes with Terminal Hydroxo and Oxo Ligands: Probing Reactivity via O-H Bond Dissociation Energies. *J. Am. Chem. Soc.* **2003**, *125*, 13234−13242.
(25) VanNatta, P. E.; Ramirez, D. A.; Velarde, A. R.; Ali, G.; Kieber-Emmons, M. T. Exceptionally High O-H Bond Dissociation Free Energy of a Dicopper(II) μ-Hydroxo Complex and Insights into the Geometric and Electronic Structure Origins Thereof. *J. Am. Chem. Soc.* **2020**, *142*, 16292−16312.
(26) Baumgarten, M.; Winscom, C. J.; Lubitz, W. Probing the surrounding of a cobalt(II) porphyrin and its superoxo complex by EPR techniques. *Appl. Magn. Reson.* **2001**, *20*, 35−70.
(27) Warren, J. J.; Tronic, T. A.; Mayer, J. M. Thermochemistry of Proton-Coupled Electron Transfer Reagents and Its Implications. *Chem. Rev.* **2010**, *110*, 6961−7001.
(28) Wise, C. F.; Agarwal, R. G.; Mayer, J. M. Determining Proton-Coupled Standard Potentials and X-H Bond Dissociation Free Energies in Nonaqueous Solvents Using Open-Circuit Potential Measurements. *J. Am. Chem. Soc.* **2020**, *142*, 10681−10691.
(29) Warren, J. J.; Mayer, J. M. Predicting organic hydrogen atom transfer rate constants using the Marcus cross relation. *Proc. Nat. Acad. Sci. U. S. A.* **2010**, *107*, 5282−5287.
(30) Abraham, M. H.; Grellier, P. L.; Prior, D. V.; Morris, J. J.; Taylor, P. J. Hydrogen Bonding. Part 10. A Scale of Solute Hydrogen-bond Basicity using log K Values for Complexation in Tetrachloromethane. *J. Chem. Soc. Perkin Trans. 2* **1990**, 521−529.
(31) Abraham, M. H.; Grellier, P. L.; Prior, D. V.; Duce, P. P.; Morris, J. J.; Taylor, P. J. Hydrogen Bonding. Part 7. A Scale of Solute Hydrogen-bond Acidity based on log K Values for Complexation in Tetrachloromethane. *J. Chem. Soc. Perk. Trans. 2* **1989**, 699−711.
(32) Borges dos Santos, R. M.; Martinho Simões, J. A. Energetics of the O−H in Phenol and Substituted Phenols: A Critical Evaluation of Literature Data. *J. Phys. Chem. Ref. Data* **1998**, *27*, 707−739.
(33) Mondal, B.; Neese, F.; Ye, S. Control in the Rate-Determining Step Provides a Promising Strategy to Develop New Catalysts for CO_2 Hydrogenation: A Local Pair Natural Orbital Coupled Cluster Theory Study. *Inorg. Chem.* **2015**, *54*, 7192−7198.
(34) Mondal, B.; Neese, F.; Ye, S. Toward Rational Design of 3d Transition Metal Catalysts for CO2 Hydrogenation Based on Insights into Hydricity-Controlled Rate-Determining Steps. *Inorg. Chem.* **2016**, *55*, 5438−5444.
(35) Sawyer, D. T. *Oxygen Chemistry*; Oxford University Press: New York, 1991.
(36) Andrieux, C. P.; Hapiot, P.; Savéant, J.-M. Mechanism of Superoxide Ion Disproportionation in Aprotic Solvents. *J. Am. Chem. Soc.* **1987**, *109*, 3768−3775.
(37) Borden, W. T.; Hoffmann, R.; Stuyver, T.; Chen, B. Dioxygen: What Makes This Triplet Diradical Kinetically Persistent? *J. Am. Chem. Soc.* **2017**, *139*, 9010−9018.
(38) Breneman, C. M.; Wiberg, K. B. Determining Atom-Centered Monopoles from Molecular Electrostatic Potentials. The Need for High Sampling Density in Formamide Conformational Analysis. *J. Comput. Chem.* **1990**, *11*, 361−373.
(39) Zhang, Y.-X.; Du, D.-M.; Chen, X.; Lü, S.-F.; Hua, W.-T. Enantiospecific Synthesis of Pyridinylmethyl Pyrrolidinemethanols and Catalytic Asymmetric Borane Reduction of Prochiral Ketones. *Tetrahedron: Asymmetry* **2004**, *15*, 177−182.
(40) Mader, E. A.; Larsen, A. S.; Mayer, J. M. Hydrogen Atom Transfer from Iron(II)-Tris[2,2′-bi(tetrahydropyrimidine)] to TEMPO: A Negative Enthalpy of Activation Predicted by the Marcus Equation. *J. Am. Chem. Soc.* **2004**, *126*, 8066−8067.
(41) Park, J. K.; Lee, H. G.; Bolm, C.; Kim, B. M. Asymmetric Diethyl- and Diphenylzinc Additions to Aldehydes by Using a Fluorine-Containing Chiral Amino Alcohol: A Striking Temperature Effect on the Enantioselectivity, a Minimal Amino Alcohol Loading, and an Efficient Recycling of the Amino Alcohol. *Chem.—Eur. J.* **2005**, *11*, 945−950.
(42) Stoll, S.; Schweiger, A. EasySpin, a comprehensive software package for spectral simulation and analysis in EPR. *J. Magn. Reson.* **2006**, *178*, 42−55.
(43) Neese, F. Software update: the ORCA program system, version 4.0. *WIREs Comput. Mol. Sci.* **2018**, *8*, e1327.
(44) Perdew, J. P.; Burke, K.; Emzerhof, M. Generalized Gradient Approximation Made Simple. *Phys. Rev. Lett.* **1996**, *77*, 3865−3868.
(45) Grimme, S.; Ehrlich, S.; Goerigk, L. Effect of the Damping Function in Dispersion Corrected Density Functional Theory. *J. Comput. Chem.* **2011**, *32*, 1456−1465.

https://doi.org/10.1021/jacsau.2c00268
JACS Au 2022, 2, 1899−1909

(46) Grimme, S.; Antony, J.; Ehrlich, S.; Krieg, H. A consistent and accurate ab initio parametrization of density functional dispersion correction (DFT-D) for the 94 elements H-Pu. *J. Chem. Phys.* **2010**, *132*, 154104.
(47) Weigend, F.; Ahlrichs, R. Balanced basis sets of split valence, triple zeta valence and quadruple zeta valence quality for H to Rn: Design and assessment of accuracy. *Phys. Chem. Chem. Phys.* **2005**, *7*, 3297−3305.
(48) Schäfer, A.; Huber, C.; Ahlrichs, R. Fully optimized contracted Gaussian basis sets of triple zeta valence quality for atoms Li to Kr. *J. Chem. Phys.* **1994**, *100*, 5829−5835.
(49) Schäfer, A.; Huber, C.; Ahlrichs, R. Fully optimized contracted Gaussian basis sets for atoms Li to Kr. *J. Chem. Phys.* **1992**, *97*, 2571−2577.
(50) Barone, V.; Cossi, M. Quantum Calculation of Molecular Energies and Energy Gradients in Solution by a Conductor Solvent Model. *J. Phys. Chem. A* **1998**, *102*, 1995−2001.
(51) Weigend, F. Accurate Coulomb-fitting basis sets for H to Rn. *Phys. Chem. Chem. Phys.* **2006**, *8*, 1057−1065.
(52) Neugebauer, J.; Hess, B. A. Fundamental vibrational frequencies of small polyatomic molecules from density-functional calculations and vibrational perturbation theory. *J. Chem. Phys.* **2003**, *118*, 7215−7225.
(53) Bühl, M.; Reimann, C.; Pantazis, D. A.; Bredow, T.; Neese, F. Geometries of Third-Row Transition-Metal Complexes from Density-Functional Theory. *J. Chem. Theory Comput.* **2008**, *4*, 1449−1459.
(54) Staroverov, V. N.; Scuseria, G. E.; Tao, J.; Perdew, J. P. Comparative assessment of a new nonempirical density functional: Molecules and hydrogen-bonded complexes. *J. Chem. Phys.* **2003**, *119*, 12129−12137.
(55) Becke, A. D. Density-functional thermochemistry. III. The role of exact exchange. *J. Chem. Phys.* **1993**, *98*, 5648−5652.
(56) Lee, C.; Yang, W.; Parr, R. G. Development of the Colle-Salvetti correlation-energy formula into a functional of the electron density. *Phys. Rev. B* **1988**, *37*, 785−789.
(57) Becke, A. D. Density-functional exchange-energy approximation with correct asymptotic behavior. *Phys. Rev. A* **1988**, *38*, 3098−3100.
(58) Perdew, J. P. Density-functional approximation for the correlation energy of the inhomogeneous electron gas. *Phys. Rev. B* **1986**, *33*, 8822−8824.
(59) Hellweg, A.; Hattig, C.; Hofener, S.; Klopper, W. Optimized accurate auxiliary basis sets for RI-MP2 and RI-CC2 calculations for the atoms Rb to Rn. *Theor. Chem. Acc.* **2007**, *117*, 587−597.
(60) Riplinger, C.; Neese, F. An efficient and near linear scaling pair natural orbital based local coupled cluster method. *J. Chem. Phys.* **2013**, *138*, 034106.
(61) Riplinger, C.; Sandhoefer, B.; Hansen, A.; Neese, F. Natural triple excitations in local coupled cluster calculations with pair natural orbitals. *J. Chem. Phys.* **2013**, *139*, 134101.

https://doi.org/10.1021/jacsau.2c00268
JACS Au 2022, 2, 1899−1909